An Integrated Boost Active Bridge Based Secondary Inductive Power Transfer Converter

Gaurav R. Kalra, *Student Member, IEEE*, Baljit S. Riar, and Duleepa J. Thrimawithana, *Senior Member, IEEE*

***Abstract*—Due to its inherent safety, robustness, and high efficiency, inductive power transfer (IPT) technology is highly suitable for the implementation of wireless electric vehicle (EV) chargers. In addition, IPT-based EV chargers can provide consistent vehicle-to-grid services, opportunistic charging, and in-motion/dynamic charging. However, designing such systems to adhere to applicable standards, while ensuring constant power transfer, and high efficiency, remains a challenge. For example, to meet the requirements outlined by SAE J2954, a wireless charger should tolerate a coupling change from 10% to 30% and a battery voltage variation from 280 to 420 V. A boost active bridge (BAB) converter presented in previous work was shown as a suitable solution; however, this system utilized two additional dc inductors. As such, this article presents a BAB converter, which integrates the current splitting functionality previously achieved using two dc inductors into a Double D magnetic coupler. This achieves a reduction in the magnetic volume of approximately 70%. Analysis of the proposed converter together with detailed design guidelines to maximize power transfer efficiency for a system designed to meet the SAEJ2954 specifications is also presented. Experimentally obtained efficiencies from a 7-kW prototype system showed minimal variation over the full range of loading conditions, ranging between 94.2% and 92%.**

***Index Terms*—Electric vehicle charger, inductive power transfer (IPT), wireless power transfer, zero voltage switching.**

NOMENCLATURE

IBAB	Secondary Integrated Boost Active Bridge converter.
L_{pt} and L_{st}	Primary and secondary magnetic coupler self-inductance.
L_{pi} and L_{si}	Primary and secondary $LCCL$/LCL input inductor self-inductance.
C_p and C_s	Primary and secondary $LCCL$/LCL parallel tuning capacitance.
C_{pt}	Primary $LCCL$ series tuning capacitance.
L_s	Secondary side dc inductor.
M	Mutual inductance between the primary and secondary magnetic couplers.
k	Coupling factor between the primary and secondary magnetic couplers.
γ	Secondary magnetic coupler detuning factor.
V_p and V_s	Primary dc-link voltage and EV battery voltage.
V_{pi} and V_{si}	Ouput voltages of the primary and secondary converter, respectively.
ϕ_p	Primary side phase shift modulation in rad.
D_s	secondary side duty-cycle modulation in %.
ω_{sw}	Primary and secondary converter switching frequency in rads^{-1}.
I_{pt} and I_{st}	Current flowing through the primary and secondary magnetic couplers, respectively.
I_{si}	Current sourced by each leg of the IBAB converter.
$I_{si\text{dm}}$	Differential-mode component of I_{si} and is composed of a real and a reactive component I_{siR} and I_{siX}, respectively.
$I_{si\text{cm}}$	Common-mode component of I_{si} and is composed of a dc and an ac component $I_{si\text{cmDC}}$ and $\Delta I_{si\text{cm\_}pk}$, respectively.
I_h	Harmonic component of I_{si}.
I_s	Current flowing through the dc inductor L_s.

Manuscript received August 6, 2019; revised December 1, 2019 and February 5, 2020; accepted March 25, 2020. Date of publication April 2, 2020; date of current version July 31, 2020. Recommended for publication by Associate Editor M. Vitelli. *(Corresponding author: Gaurav Kalra.)*

Gaurav R. Kalra and Duleepa J. Thrimawithana are with the Department of Electrical and Computer Engineering, The University of Auckland, Auckland 1010, New Zealand (e-mail: gkal280@aucklanduni.ac.nz; d.thrimawithana@auckland.ac.nz).

Baljit S. Riar is with the United Technologies Research Center, East Hartford, CT 06108 USA (e-mail: riarbalj1@utrc.utc.com).

Color versions of one or more of the figures in this article are available online at https://ieeexplore.ieee.org.

Digital Object Identifier 10.1109/TPEL.2020.2984784

I. INTRODUCTION

INDUCTIVE power transfer (IPT) has fast become the preferred wireless power transfer technology to deliver high levels of power ($\leq$50 kW) over short distances ($\leq$400 mm) [1]–[3]. This preference is highlighted by the rapid uptake of the IPT technology in automotive, consumer, medical, and industrial applications, such as charging mobile devices, powering automated guided vehicles (AGVs) and charging electric vehicles (EVs) [4]–[6]. Among these applications, EV charging is regarded as one the most disruptive applications of IPT technology. IPT-based EV chargers provide significant benefits over their wired counterparts while being just as efficient [7]–[10]. These not only include the inherent advantages of safety and convenience, but also the facilitation of consistent vehicle-to-grid (V2G) services, opportunistic charging, and in-motion/dynamic charging [11]–[14]. These benefits have the potential to aid the uptake of EVs around the globe and therefore help transition to a more environmentally sustainable transportation sector.

A typical IPT-based EV charging system consists of a grid-tied converter, which derives a steady dc-link voltage, V_p, from a single or three-phase grid connection. As shown in Fig. 1, V_p feeds the primary IPT inverter, which drives the primary

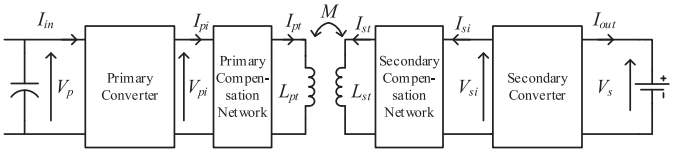

Fig. 1. Conceptual block diagram of an IPT-based EV charging system.

magnetic coupler through a compensation network with a high-frequency voltage/current excitation. A part of the magnetic flux generated by the primary magnetic coupler induces a voltage across the secondary magnetic coupler, which in turn feeds the EV battery through a secondary compensation network and a secondary IPT converter.

One of the most challenging aspect of the design of an IPT-based EV charging system is ensuring a constant level of power transfer and a high power transfer efficiency while adhering to alignment and output voltage specifications highlighted in the applicable standards, such as SAE J2954 [15] or IEC 61980 [16], that are currently being developed. For example, recently published SAE J2954 recommended practices for a WPT2 power-class charger defines an input power from the utility grid of 7.7 kW, i.e., an output power of approximately 7 kW when a 90% grid to battery efficiency is assumed. The defined charging region encompasses +/− 75 mm in the direction parallel to the movement of the vehicle (*X*), +/− 100 mm in the perpendicular direction (*Y*), and +/− 100 mm of variation in vehicle height (*Z*). For a system employing Double D (DD) magnetic couplers [17] recommended in SAE J2954, when the secondary coupler is furthest from the primary coupler, k drops to about 10%, while they are closest to each other k is about 30%. SAE J2954 also defines that the wireless EV charger should be capable of delivering up to rated power when the EV battery is fully depleted (280 V) as well as close to full charge (420 V).

The most straightforward approach to cater to such an extensive range of operating conditions is to employ a full-bridge with phase-shift control as the primary IPT converter and a simple full-wave diode rectifier as the secondary converter [3], [8]–[10], [18]. In the case of an $LCL/LCCL$ primary compensation network, the full-bridge is typically operated at its maximum phase-shift at the lowest k to minimize switching losses and deliver rated power to a fully depleted battery. However, the system will invariably suffer from increased losses when operating conditions change as the full-bridge needs to be controlled to regulate the power flow leading to hard switching [19]. Furthermore, since Volt–Amperes (VA) in the secondary magnetic coupler cannot be directly controlled, the system will operate at suboptimal ac–ac efficiencies under most conditions.

The efficiency of an IPT system over a wide load range can be enhanced by the use of tunable matching networks (TMNs). However, since the TMNs are typically composed of an electronically controlled reactance; and require complex control algorithms, the component count and cost is high [20].

To allow for direct control of the VA in the secondary magnetic coupler and therefore allow the system to operate under maximum ac–ac efficiency conditions, boost or buck type secondary side controllers have been proposed [21]–[24]. Secondary side regulation reduces the stress on the primary full-bridge converter and extends its soft-switching range. However, hard-switching and high-current stresses on the secondary side converter lead to significantly reduced efficiencies when the secondary magnetic coupler is required to operate under low VAs, i.e., at high coupling positions and high battery voltages.

Interleaved versions of these converters have also been proposed to reduce current stresses [25], similar to the recommended architecture for a WPT2 power-class system in SAE J2954. Nevertheless, hard-switching remains a significant deficiency. High efficiency over a wide load range was achieved using dual-side control in [26], where a full-bridge was employed on the primary side and an active rectifier on the secondary. However, since the system was designed to transfer 3 kW when operating with a 400 V dc-link and a switching frequency of 35 kHz, the impact of hard-switching and conduction losses on the system efficiency was minimal. Thus, a significant reduction in efficiency as well as an increase in thermal management requirements would be expected when operating at a SAE J2954 compliant switching frequency of 85 kHz and a power level of 7 kW.

To address the shortcomings above, a wireless EV charger that employs synchronized boost active bridge (BAB) converters on both the primary and secondary sides was proposed in [27]. A BAB can generate an ac voltage, which is either higher or lower than the supply voltage, thus enabling improved control flexibility and reduced current stresses. The system proposed in [27] can also achieve ZVS or ZCS over a wide range of operating conditions. As such, the BAB-based IPT system achieved almost constant efficiency between 500 W to 3.5 kW at a fixed coupling position and battery voltage, but at the cost of two additional dc inductors in each converter. These additional components are especially problematic on the secondary side as the available space is severely constrained.

This article proposes the use of a DD secondary magnetic coupler together with a single dc inductor to replace the two dc inductors found in a BAB and thus reduce its cost and the size. The current splitting functionality previously achieved using the two dc inductors is now integrated into the DD coupler itself. Although a single dc inductor is still required, the ripple-current is largely reduced as only the common-mode voltage is applied across it. Therefore, the magnetic volume required by the dc inductor of the proposed secondary BAB, which is referred to as an integrated BAB (IBAB) in this article, will be about 70% lower in comparison to a traditional BAB.

This article aims to provide a comprehensive analysis of the proposed secondary BAB converter together with detailed design guidelines to maximize power-transfer efficiency for a system designed to meet the SAE J2954 WPT2 power-class specifications. Section II of this article describes the configuration and control scheme of the proposed BAB-based wireless EV charging system, followed by a description of the magnetic couplers utilized in Section III. Section IV provides a detailed mathematical model of the system, as well as design equations required to size passive components. The mathematical model is extended to predict conduction losses and the soft-switching conditions in Section V. Using these improved models, system,

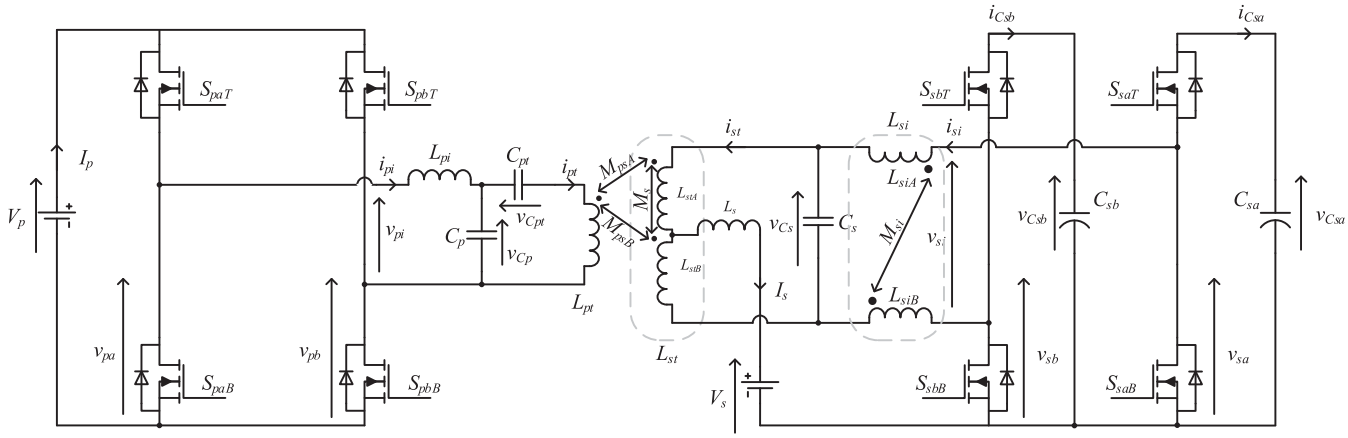

Fig. 2. Schematic of the proposed system utilizing an IBAB as the secondary converter.

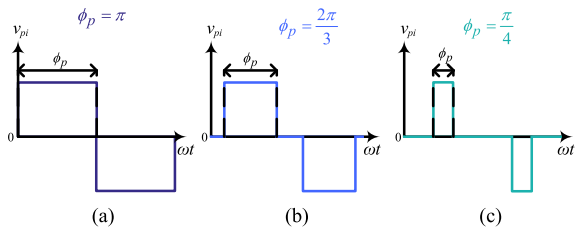

Fig. 3. Output voltage of the primary full-bridge utilizing phase shift control at (a) $\phi_p = \pi$, (b) $\phi_p = 2\pi/3$, and (c) $\phi_p = \pi/4$.

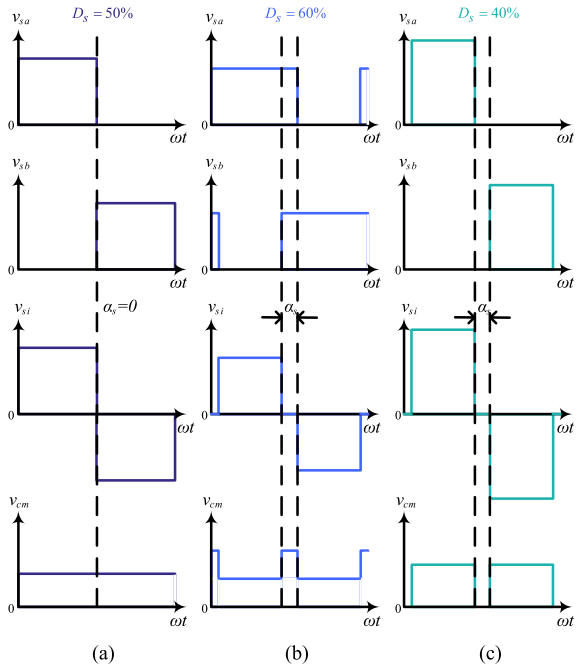

Fig. 4. Voltages produced the IBAB utilizing the proposed switching scheme at (a) 50%, (b) 60% and (c) 40% duty-cycles.

and control parameters are determined to achieve maximum power transfer efficiencies under each operating condition. To verify the developed models and validate the viability of the proposed EV charging system, a 7-kW prototype system is developed and experimental waveforms and efficiencies are captured over the full operating range defined by the SAE J2954 standard.

II. Converter Functional Description

The proposed IPT system is shown in Fig. 2, where the primary side consists of a standard full-bridge converter whose output feeds an $LCCL$ compensated DD magnetic coupler, L_{pt} [28]. The input voltage to the primary converter, which is typically derived from a single- or three-phase grid connection is modeled, as an ideal voltage source, V_p. Fig. 3 shows the output voltage of the primary full-bridge converter v_{pi}, which can be regulated by adjusting the phase shift between the two bridge legs ϕ_p [19]. The secondary side utilizes a novel IBAB converter, which drives a center-tapped DD magnetic coupler, L_{st}, through an LCL compensation network. The center-tap of L_{st} is connected to the EV battery, which is modeled as an ideal voltage source V_s, through a dc inductor, L_s. Similar to a BAB, the IBAB converter is constructed using two half-bridge converters. Half-bridge converter "a," B_{sa}, is made up from switch pair S_{saT} and S_{saB}, while half-bridge converter "b," B_{sb}, is made up from switch pair S_{sbT} and S_{sbB}. The dc-bus capacitors C_{sa} and C_{sb} are connected across the dc sides of B_{sa} and B_{sb}, respectively. The outputs of B_{sa} and B_{sb} are connected to the positive and negative terminals of the LCL compensation network, respectively.

As illustrated by Fig. 4, B_{sa} and B_{sb} are both switched in a complementary manner with duty-cycles D_{sa} and D_{sb}, respectively, and with a fixed 180^0 phase difference between them. Thus, this arrangement forms an interleaved, bidirectional buck–boost converter between V_s and C_{sa}; as well as V_s and C_{sb}. By applying the volt-second rule to the inductive impedance network between V_s and the dc-bus capacitors, the voltages V_{Csa} and V_{Csb} can be related to D_{sa} and D_{sb} as

$$D_{sa}V_{Csa} = D_{sb}V_{Csb} = V_s. \tag{1}$$

Accordingly, operating a half-bridge at a duty-cycle of 50% will result in approximately double the battery voltage across the dc-bus capacitors. Reducing or increasing the duty-cycles results in a higher or lower voltage, respectively, across the corresponding half-bridge converter, as shown by Fig. 4.

This circuit arrangement also creates a quasi-full-bridge converter whose output is v_{si} and is defined by the voltage difference between v_{sa} and v_{sb}. Accordingly, using (1), the average of v_{si} over one switching period can be expressed as

$$\begin{aligned}\langle v_{si}\rangle &= \langle v_{sa}\rangle - \langle v_{sb}\rangle \\ &= D_{sa}V_{Csa} - D_{sb}V_{Csb} = 0. \end{aligned} \tag{2}$$

Thus, unlike a traditional full-bridge converter v_{si} produced by the IBAB presents a zero dc-bias, even when D_{sa} and D_{sb} are not equal. As such, the LCL compensation network can be directly driven by the IBAB, eliminating the need for the dc-blocking capacitor typically found in a full-bridge driven system. Moreover, it is this feature that allows for the integration of the current splitting functionality into the DD coupler itself, as there is a path for the dc current through the LCL network. Typically, in order to produce a symmetric v_{si} to drive the LCL network, B_{sa} and B_{sb} are operated with equal duty-cycles, i.e., $D_{sa} = D_{sb} = D_s$.

As shown by Fig. 4, the magnitude of v_{si} is controlled using D_s, but through two different mechanisms. First, as discussed earlier and given by (1), D_s controls the voltages across the dc-bus capacitors and therefore the amplitude of v_{si}. Second, due to voltage cancellation, D_s simultaneously controls α_s, i.e., the duration of the 0 V level associated with v_{si}. α_s can be derived in radians as

$$\alpha_s = \pi\left|1 - 2D_s\right|. \tag{3}$$

Overall, the combination of these two mechanisms enables the IBAB to control the magnitude of v_{si} with considerably reduced control effort, which in turn enables a greater ZVS region. The proposed IBAB-based system is analyzed further with detailed mathematical models in Section III.

III. Mathematical Model

As shown by Fig. 4, the proposed IBAB converter produces a differential-mode output, $v_{si} = v_{sa} - v_{sb}$, and a common-mode output, $v_{\text{cm}} = 0.5(v_{sa} + v_{sb})$. In order to simplify the following analysis, each output and their respective equivalent circuits can be analyzed independently.

Due to the high-order, low-pass nature of $LCCL$-LCL network, the majority of the power is delivered at the fundamental switching frequency, $\omega_{\text{sw}} = 2\pi f_{\text{sw}}$. Therefore, the power transfer is modeled using a fundamental-frequency, phasor-domain approximation. However, to analyze soft-switching conditions, this analysis is extended to include the impact of harmonics produced by the IBAB.

As discussed in Section IV, the inductance of an SAE-J2954 compliant primary magnetic coupler remains relatively constant throughout the operating region. Thus, the following analysis is further simplified by developing a model that only captures the secondary side detuning effects.

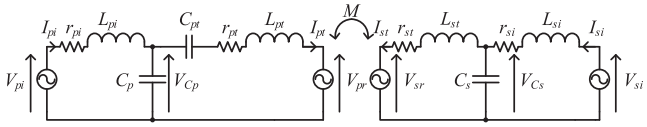

Fig. 5. Equivalent phasor domain representation of the compensation networks.

A. Power Transfer Model

First, the differential-mode output produced by the IBAB is considered in order to develop a model for power transfer. The phasor-domain equivalent circuit used for this analysis is illustrated in Fig. 5. Here, the secondary magnetic coupler is modeled as a lumped inductor, L_{st}, which has a value equal to $L_{stA} + L_{stB} + 2M_s$. Similarly, the input inductor used in the secondary LCL compensation network is modeled as L_{si}, with a value of $L_{siA} + L_{siB} + 2M_{si}$. The effective mutual inductance, M, between L_{pt} and L_{st} in Fig. 5 can be calculated as $M_{psA} + M_{psB}$. The primary and the secondary compensation networks are only tuned at a specific position of the secondary coupler within the operating region specified by SAE J2954. At this position, the self-inductance of the secondary coupler can be regarded as $L_{st}^{'}$ and therefore

$$\omega_{\text{sw}}^2 = \frac{1}{L_{pi}C_p} = \frac{1}{\left(L_{pt} - 1/\omega_{\text{sw}}^2 C_{pt}\right)C_p} = \frac{1}{L_{si}C_s} = \frac{1}{L_{st}^{'}C_s}. \tag{4}$$

The self-inductance of the secondary coupler at an arbitrary position within the operating region is expressed as $L_{st} = L_{st}^{'}\gamma$ to account for the detuning effects.

The output voltages of the primary full-bridge converter and the secondary IBAB v_{pi} and v_{si}, respectively, are modeled by their fundamental-frequency components, and are given as

$$V_{pi} = V_p\frac{2\sqrt{2}}{\pi}\sin\left(\frac{\phi_p}{2}\right) \tag{5}$$

$$V_{si} = V_s\frac{2\sqrt{2}}{D_s\pi}\cos\left(\frac{\alpha_s}{2}\right)\angle\theta \tag{6}$$

where θ represents the phase-delay between V_{pi} and V_{si}, and is fixed at 90° to maximize power transfer [11], [29].

The primary and secondary magnetic coupler currents can be calculated as

$$I_{pt} = \frac{V_{pi}}{j\omega_{\text{sw}}L_{pi}} \text{ and } I_{st} = \frac{V_{si}}{j\omega_{\text{sw}}L_{si}}. \tag{7}$$

The resulting voltages induced on each magnetic coupler can therefore be given as

$$V_{pr} = j\omega_{\text{sw}}MI_{st} \text{ and } V_{sr} = j\omega_{\text{sw}}MI_{pt} \tag{8}$$

where $M = k\sqrt{L_{pt}L_{st}}$. Applying the Norton transformation, the voltage induced across the secondary coupler in Fig. 5, can be represented as a current source I_{sr}, as shown in Fig. 6, where Z_{sr} is given by

$$Z_{sr} = \frac{j\omega_{\text{sw}}L_{st}^{'}\gamma}{1-\gamma}. \tag{9}$$

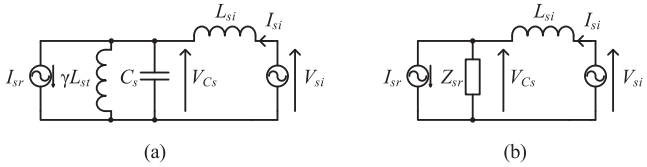

Fig. 6. Norton equivalent secondary compensation circuit.

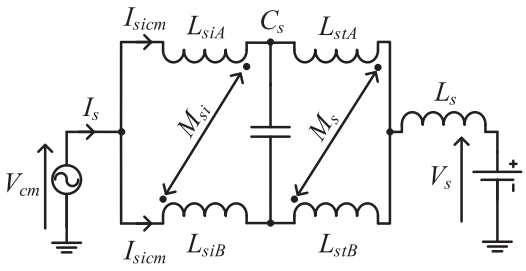

Fig. 7. Common-mode equivalent circuit configuration.

When $\gamma \neq 1$, Z_{sr} has a finite impedance and thus the differential-mode component of I_{si}, I_{sidm}, is composed of two orthogonal components. The component of I_{sidm} that is in phase with V_{si} is I_{siR}, and the orthogonal component is I_{siX}, i.e., $|I_{\mathrm{sidm}}|^2 = I_{siR}^2 + I_{siX}^2$. Using Fig. 6, I_{siR} is derived as

$$I_{siR} = \frac{MI_{pt}}{L_{st}^{'}\gamma}. \tag{10}$$

I_{siX}, which is given below, does not contribute to the real power delivered, but it increases the VA rating of the secondary converter

$$I_{siX} = \frac{V_{si}}{j\omega_{\mathrm{sw}}\left(L_{si} + \frac{L_{st}^{'}\gamma}{1-\gamma}\right)}. \tag{11}$$

Therefore, the power delivered to the EV battery can be derived as

$$P_{\mathrm{out}} = \frac{8V_pV_sM}{\omega_{\mathrm{sw}}L_{pi}L_{st}^{'}D_s\pi^2}\sin\left(\frac{\phi_p}{2}\right)\cos\left(\frac{\alpha_s}{2}\right). \tag{12}$$

Accordingly, when designing a power-flow controller either ϕ_p or D_s, or a combination of both can be utilized. However, ϕ_p and D_s directly impact the ac–ac efficiency of the system as well as the switching and conduction losses. Therefore, in order to maximize the efficiency, it is crucial to operate at a preferable combination of ϕ_p and D_s at each position of the secondary coupler as discussed in the following sections.

B. Common-Mode Output Analysis

Analysis of the common-mode output of the IBAB converter allows the development of models which can be used to size the dc inductor and to understand its impact on the device losses. Fig. 7 shows the common-mode equivalent circuit of the IBAB converter used in the secondary side. I_s represents the common-mode current sourced by the common-mode voltage source V_{cm}, which flows through the secondary LCL network and the dc inductor L_s. I_s is composed of a dc current responsible for power delivery, $I_{s\mathrm{DC}}$, and a ripple component at twice the switching frequency, ΔI_{s_pk}. $I_{s\mathrm{DC}}$ is equal to P_{out}/V_s, while ΔI_{s_pk} is dependent on the equivalent common-mode inductance L_{cm}. Assuming $L_{stA} = L_{stB}$, L_{cm} can be approximated based on Fig. 7 as

$$L_{\mathrm{cm}} = \frac{L_{stA} - M_s}{2} + L_s. \tag{13}$$

Since it is likely that $L_s \gg \frac{L_{stA}-M_s}{2}$, L_{cm} can be approximated as L_s. Based on this assumption, ΔI_{s_pk} can be given as

$$\Delta I_{s\_pk} = \begin{cases} \frac{V_s(1-2D_s)}{4f_{\mathrm{sw}}L_s} & D_s \leq 0.5 \\ \frac{V_s(1-D_s)(1-2D_s)}{D_s f_{\mathrm{sw}}L_s} & D_s > 0.5. \end{cases} \tag{14}$$

Thus, using (14), L_s can be determined for a desired peak ripple to average current ratio $\Delta_s = \Delta I_{s\_pk}/I_{s\mathrm{DC}}$.

Equations (13) and (14) also highlight some key advantages of the proposed IBAB. First, the dv/dt applied across the dc inductor is much lower than if it was placed across the differential-mode voltage, as is the case with a standard BAB. Thus, a physically smaller inductor can be used for the same amount of ripple current. Moreover, when operating with a duty-cycle of 50% the ripple current is approximately zero. Second, if the secondary magnetic coupler has sufficient leakage inductance between the two D-shaped windings, the requirement for the dc inductor can be eliminated, while still maintaining a low common-mode ripple current.

As an example, the minimum required inductance of L_s can be calculated as a function of the maximum allowable Δ_s when $D_{s\_\min} \leq 0.5$ as per

$$L_s = \frac{V_{s\_\min}^2(1-2D_{s\_\min})}{4P_{\mathrm{out}}f_{\mathrm{sw}}\Delta_s}. \tag{15}$$

Now, consider a traditional BAB converter which uses two separate dc inductors L_{sa} and L_{sb}, to connect each half-bridge to the EV battery as in [27]. The minimum required inductance for this system can also be calculated as a function of Δ_s as per

$$L_{sa} = L_{sb} = \frac{V_{s\_\min}^2(1-D_{s\_\min})}{P_{\mathrm{out}}f_{\mathrm{sw}}\Delta_s}. \tag{16}$$

Since the volume of an inductor is proportional to the peak energy stored by it, the reduction in magnetic volume achieved by the IBAB topology in comparison to the BAB topology can be expressed by combining (15)–(17) as

$$\kappa = \frac{L_s\hat{I_s^2}}{2L_{sa}\hat{I_{L_{sa}}^2}} = \frac{(1-2D_{s\_\min})}{2(1-D_{s\_\min})}. \tag{17}$$

As such, a system designed to operate at a minimum duty-cycle of 30% would require 70% lower magnetic volume if using the IBAB topology as opposed to a traditional BAB topology.

Due to the symmetrical circuit arrangement, I_s is divided equally between each leg of the IBAB. Thus, the common-mode component of current through each leg of the IBAB is defined as $I_{si\mathrm{cm}} = I_s/2$. Furthermore, the dc and ripple components of $I_{si\mathrm{cm}}$ can be given as $I_{si\mathrm{cmDC}} = I_{s\mathrm{DC}}/2$ and $\Delta I_{si\mathrm{cm}\_pk} = \Delta I_{s_pk}/2$, respectively.

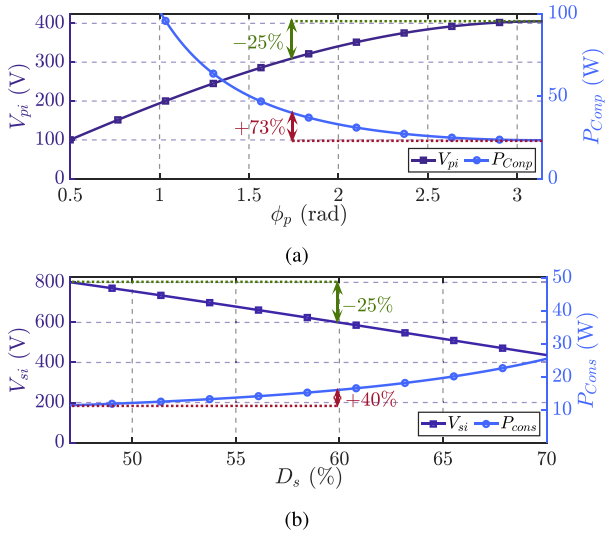

Fig. 8. Switching device conduction loss when $P_{\text{out}} = 7$ kW of the (a) primary full-bridge as a function of ϕ_p when $V_p = 450$ V. (b) Secondary IBAB as a function of D_s when $V_s = 420$ V.

$I_{si\text{cm}}$ also flows through L_{st} and L_{si}, which can be seen as the main drawback of an IBAB converter. However, as discussed above, $I_{si\text{cm}}$ is mainly dc. And since the dc resistances of L_{st} and L_{si} are significantly smaller than their ac resistances [30], the additional conduction loss due to $I_{si\text{cm}}$ can be neglected. Furthermore, since L_{siA} and L_{siB} are tightly coupled, there is almost zero net flux produced in the core due to the common-mode current. Thus, as is the case with a traditional BAB, the magnetic losses in L_{si} are only attributed to the differential mode current flowing through it. Similarly, due to the construction of the DD coupler, the mutual-flux generated by $I_{si\text{cm}}$ flowing through each D-shaped winding also negate each other.

C. Conduction Loss Analysis

Assuming that the conduction loss associated with the primary full-bridge is mainly due to the fundamental component of I_{pi}, it can be approximated as

$$P_{\text{conp}} = 2I_{pi}^2 R_{ds(\text{on})} = 2\left(\frac{P_{\text{out}}}{V_{pi}}\right)^2 R_{ds(\text{on})} \tag{18}$$

where $R_{ds(\text{on})}$ is the ON resistance of the switching device. Assuming that I_{siR} and $I_{si\text{cmDC}}$ dominate the conduction loss associated with the secondary IBAB, it can be approximated as

$$\begin{aligned} P_{\text{cons}} &= 2\left[I_{siR}^2 + I_{si\text{cmDC}}^2\right] R_{ds(\text{on})} \\ &= 2\left[\left(\frac{P_{\text{out}}}{V_{si}}\right)^2 + \left(\frac{P_{\text{out}}}{2V_s}\right)^2\right] R_{ds(\text{on})}. \end{aligned} \tag{19}$$

As k or V_s vary, either ϕ_p, D_s or both need to adjusted to maintain a constant output power level. According to (18) and (19), adjusting either of these control parameter will have an impact on device conduction losses. Using (18), Fig. 8(a) shows P_{conp} as a function of ϕ_p when $P_{\text{out}} = 7$ kW and $V_p = 450$ V. On the other hand, as per (19), Fig. 8(b) shows P_{cons} as a function of D_s when $P_{\text{out}} = 7$ kW and $V_s = 420$ V. As apparent, when both sides are using the same device ($R_{ds} = 38$ mΩ), the conduction losses on the IBAB converter are lower for all operating condition. Furthermore, the rate of increase of power loss due to modulation is much lower for the IBAB converter in comparison to the primary full-bridge. For example, as illustrated by Fig. 8, modulating the full-bridge to reduce V_{pi} by 25% results in a 73% increase in P_{conp}, while modulating the IBAB to reduce V_{si} by 25% only results in a 40% increase in P_{cons}. Since both these options in effect achieve the same outcome, it is advantageous to use the IBAB to handle bulk of the power regulation, while maintaining ϕ_p close to 180° on the primary side.

D. ZVS and Operating Regions

Since D_{sa} and D_{sb} are equal, if B_{sa} achieves ZVS turn-ON for both switches, so will B_{sb}. As such, the following analysis investigates the switching characteristics of B_{sa} to obtain the ZVS switching range of the IBAB converter.

The fundamental condition required to achieve a ZVS turn-ON is the complete discharge/charge of the intrinsic energy stored by the switching devices during the dead time. Therefore, the load current must provide sufficient energy and flow into the mid-point of a bridge-leg to achieve a ZVS turn-ON of the top switch. Similarly, the load current should flow out of the bridge-leg for the bottom switch to achieve ZVS turn-ON [31]. Typically, SiC MOSFETs widely used in IPT systems have minimal output capacitance and the time taken to discharge/charge the intrinsic energy stored by the devices is negligible. Therefore, the ZVS condition for S_{saT} of B_{sa} is defined as $I_{\text{on}} \leq 0$, whereas ZVS condition for S_{saB} is defined as $I_{\text{off}} \geq 0$. As illustrated by Fig. 9, I_{on} and I_{off} represent the currents at the instance of commutation of S_{saT} and S_{saB}, respectively, where

$$I_{\text{on}} = i_{si}\left(\frac{1 - D_s}{2f_{\text{sw}}}\right) \text{ and } I_{\text{off}} = i_{si}\left(\frac{1 + D_s}{2f_{\text{sw}}}\right) \tag{20}$$

where, as shown by Fig. 2, i_{si} is IBAB output current and includes both differential-mode and common-mode contributions. I_{on} and I_{off} can be evaluated accurately, using a complex mathematical model of i_{si} and solving it numerically [27]. However, such a complex approach abstracts the key factors contributing to ZVS. Thus, a simplified model is developed by decomposing i_{si} into its components that contribute to ZVS turn-ON and analyzing the impact of each component separately.

First, consider just the fundamental component i_{siR} and the dc component $I_{si\text{cmDC}}$. The combination of these two components at the tuned position is illustrated in Fig. 9(b) for various duty-cycles. As evident, due to $I_{si\text{cmDC}}$, i_{siR} has a positive bias, which facilitates ZVS turn-ON of S_{saB} under most conditions. Since, under most conditions $I_{\text{on}} \geq 0$, S_{saT} does not achieve ZVS turn-ON. If only considering i_{siR} and $I_{si\text{cmDC}}$, it is evident that reducing D_s below 50% helps S_{saT} to operate closer to the ZVS boundary.

The above analysis can be extended by considering the switching harmonic frequencies present in $i_{si\text{dm}}$. At these harmonic frequencies, the impedance of C_s approaches zero, thus the impedance seen by V_{si} can be approximated as $\omega_{\text{sw}} L_{si}$. Accordingly, as shown in Fig. 9(c), the peak ripple current generated

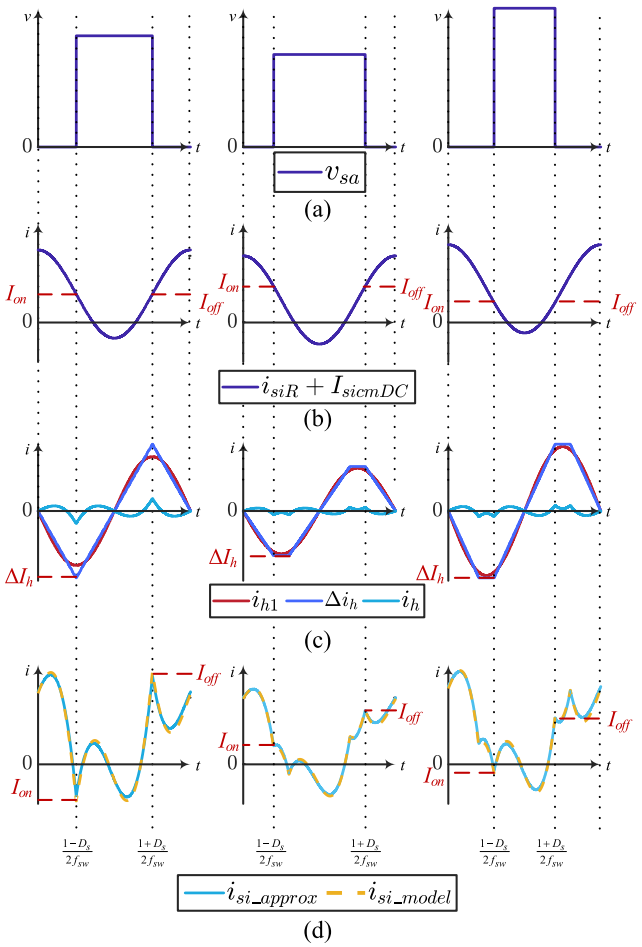

Fig. 9. Pictorial representation of the harmonic approximation method used to predict I_{on} and I_{off}.

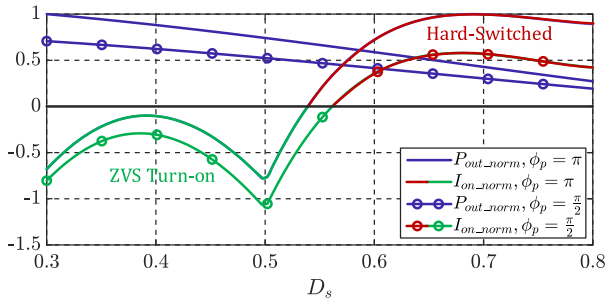

Fig. 10. I_{on} and P_o as a function of D_s normalized to their maximum values.

can be given as

$$\Delta I_h = \frac{V_s\,(\pi - \alpha_s)}{2\omega_{\text{sw}} D_s L_{si}}. \tag{21}$$

This expression contains the contribution of both the fundamental as well as the harmonic components of V_{si}. However, the above approximation is only valid for harmonic frequencies of V_{si}, and therefore the contribution of the fundamental component needs to be subtracted from (21). The contribution of the fundamental component of V_{si} in ΔI_h, which is shown by Fig. 9(c), is given as

$$I_{h1} = \frac{V_{si}}{\omega_{\text{sw}} L_{si}}. \tag{22}$$

Using (10), (12), and (20)–(22), I_{on} is approximated as

$$I_{\text{on}} = i_{si\_\text{approx}}\left(\frac{1-D_s}{2f_{\text{sw}}}\right) = \sqrt{2} I_{siR} \cos\left(\frac{1-D_s}{2f_{\text{sw}}}\right) \ldots$$
$$\ldots + \sqrt{2} I_{h1} \sin\left(\frac{1-D_s}{2f_{\text{sw}}}\right) + I_{\text{sicmDC}} - \Delta I_h. \tag{23}$$

To verify this approximation, in Fig. 9(d), the resulting time-domain waveform, i_{si_approx}, is plotted alongside one produced using the complex mathematical model in [27], i_{si_model}. For a system with specifications listed in Table II, both waveforms present excellent correlation, thus verifying the approximation. The accuracy of this approximation can be further improved by also modeling the impact of I_{siX} and $\Delta I_{si\text{cm}\_pk}$. However, the magnitudes of I_{siX} and $\Delta I_{si\text{cm}\_pk}$ are significantly lower than magnitudes of the three components analyzed above. Furthermore, typically the secondary LCL compensation network is designed such that $\gamma < 1$, and therefore both I_{siX} and $\Delta I_{si\text{cm}\_pk}$ will provide a minor improvement in the ZVS turn-ON range.

Using (23) the ZVS turn-ON conditions can be approximated. As an example, consider the system with specifications listed in Table II, which is designed to deliver maximum power when $\phi_p = \pi$ and $D_s = 30\%$. Fig. 10 shows the normalized I_{on} and P_o of this system for $\phi_p = \pi$ as well as $\phi_p = 0.5\pi$. When D_s is increased above 55% to regulate P_o to 60% of the rated value or lower, S_{saT} will lose ZVS turn-ON. This is due to two reasons: First, as evident from Fig. 9(b), increasing the duty-cycle increases the contribution of I_{siR} in I_{on}. Second, as evident from Fig. 9(c), increasing the duty-cycle reduces the magnitude of V_{si} and therefore the contribution of ΔI_h in I_{on}. Both these factors result in I_{on} moving further away from the ZVS turn-ON boundary. In order to increase the ZVS turn-ON range, ϕ_p can be used together with D_s to regulate P_o. As evident from Fig. 10, if ϕ_p is reduced to 0.5π, the ZVS range can be increased. This is because lowering ϕ_p only reduces I_{siR} and does not impact ΔI_h.

Meeting ZVS turn-ON conditions for a switch in a bridge-leg helps the complementary switch achieve soft turn-OFF. The loss incurred during a soft turn-OFF depends on the output capacitance of the switches, the load current, snubber circuitry, and the printed circuit board layout. However, the soft turn-OFF loss is significantly lower than hard-switching losses.

IV. Selection of Control Parameters

In order to highlight the benefits offered by the IBAB as a secondary side converter, a prototype system, which complies with the SAE J2954 WPT2/Z2 specifications was developed. As shown by Fig. 11, DD magnetic couplers were utilized on both the primary and secondary sides. Table I lists the experimental magnetic parameters for various location of the secondary coupler within the operating region specified by the standard. The origin of the coordinate system used in Table I is at the center of the primary magnetic coupler as shown in Fig. 11(a). While, as

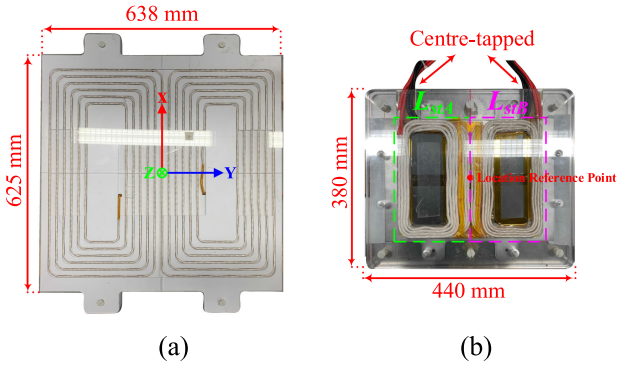

Fig. 11. Physical construction of the (a) primary and (b) secondary magnetic couplers.

TABLE I
MAGNETIC PARAMETERS

Secondary Location (X,Y,Z) (mm)	L_{pt}	L_{st}	k	γ
(0,0,125)	64.56 μH	18.28 μH	0.288	1
(0,0,145)	64.62 μH	17.87 μH	0.237	0.98
(0,0,167)	64.43 μH	17.61 μH	0.198	0.96
(75,100,167)	64.57 μH	17.61 μH	0.144	0.96
(75,100,200)	64.12 μH	17.41 μH	0.110	0.95

TABLE II
CIRCUIT PARAMETERS

Parameter	Value	ESR
L_{pi}	13.78 μH	12.3 $m\Omega$ @85 kHz
C_p	257.6 nF	2.4 $m\Omega$ @85 kHz
C_{pt}	69.55 nF	9 $m\Omega$ @85 kHz
L_{si}	17.3 μH	15.4 $m\Omega$ @85 kHz
C_s	192.4 nF	3.2 $m\Omega$ @85 kHz
L_s	253.6 μH	26.6 $m\Omega$ @DC
f_{sw}	85 kHz	—
$Switch$	$C2M0025120D$	38 $m\Omega$ @40°C

shown by Fig. 11(b), the coordinates given as (*X*,*Y*,*Z*) in Table I define the location of the center of the secondary magnetic coupler with reference to the origin. As per the WPT2/Z2 test stand, the prototype was designed to deliver rated power (7 kW) for the full range of battery voltages, i.e., 280 to 420 V, and it was assumed that the input dc-link voltage can be controlled from 350 to 450 V using the grid-tied converter [15]. A full list of system parameters and their equivalent series resistances (ESRs) measured using an *LCR* meter are provided by Table II.

As discussed in the preceding section, the control parameters ϕ_p and D_s were chosen to minimize the power loss while regulating the output power to 7, 5, and 3 kW at each location specified in Table I. In order to derive the control parameters, the mathematical model presented in Section III was extended to predict the losses associated with all the components. For example, soft-switching turn-OFF loss and the hard-switching loss of the converters were predicted using look-up tables that were developed using SPICE models.

Consider the scenario where the IBAB is required to deliver 7 kW to the EV when the secondary coupler is at (75,100,200), (0,0,167), or (0,0,145). Also, assume that the EV battery is at 420 V. When the secondary coupler is at (75,100,200) coupling is the lowest ($k = 0.11$) while when at (0,0,145) coupling is relatively high ($k = 0.237$). For each location of the secondary, the ZVS turn-ON range for both converters as a function of ϕ_p and D_s are illustrated by Fig. 12. P_o is also shown as contour lines of constant power. When operating at points encompassed within the regions highlighted in Fig. 12, all four switches of the corresponding converter achieve ZVS turn-ON. When operating outside the highlighted region, two out of the four switches of each converter achieve ZVS turn-ON. To further understand how the losses change when moving along the 7 kW contour line in Fig. 12, Fig. 13 shows the primary and secondary magnetic coupler losses, P_{Lpt} and P_{Lst}, respectively, as well as the primary and secondary converter losses, P_{Swp} and P_{Sws}, respectively.

When the secondary coupler is at (75,100,200), k is very small and therefore the input dc-link voltage is controlled to be at its highest voltage (450 V). As indicated by Figs. 12(a) and 13(a), under these conditions, both the primary and secondary converters present a large ZVS turn-ON range and low switch conduction losses due to the relatively high ϕ_p and low D_s required to maintain an output power of 7 kW. On the other hand, at this position, the losses in the magnetic couplers are at their highest due to larger I_{pt} and I_{st}. Based on this analysis, as highlighted in Fig. 13(a) by a dashed line, when operating at (75,100,200), D_s has to be set to 56% to minimize the total losses. This operating point is shown by point "A" in Fig. 12(a), which indicates that all eight switches achieve ZVS turn-ON under these conditions.

When the secondary coupler moves to (0,0,167), k increases to 0.19 and therefore the input dc-link voltage is controlled to be at its lowest voltage (350 V). However, V_{pi} and/or V_{si} should be reduced further by controlling ϕ_p and/or D_s to maintain an output power of 7 kW. As discussed earlier, and shown by Figs. 12(b) and 13(b), a reduction in V_{pi} not only leads to excessive conduction losses on the primary converter, but also results in hard-switching. Since the switch conduction losses are relatively large, the operating point "A" in Fig. 13 is chosen to achieve ZVS turn-ON for all primary switches. This ensures the total loss per switch is kept within its safe operating region. Due to the much lower conduction losses in the secondary switches, their power dissipation is well within limits even when only two switches achieve ZVS turn-ON.

As illustrated by Figs. 12(c) and 13(c), when the secondary coupler is at (0,0,145) the magnetic coupler loss is low and the overall loss is dominated by the converter losses. This is especially true if the full-bridge is required to reduce ϕ_p. However, as with the previous case, due to the lower conduction losses on the IBAB, D_s can be increased significantly to regulate the power flow, while allowing the primary converter to maintain a high ϕ_p.

The control parameters used to regulate the power transfer to 7 kW at each location of the secondary can be derived as per the above analysis, which are tabulated in Table III. Similarly, the

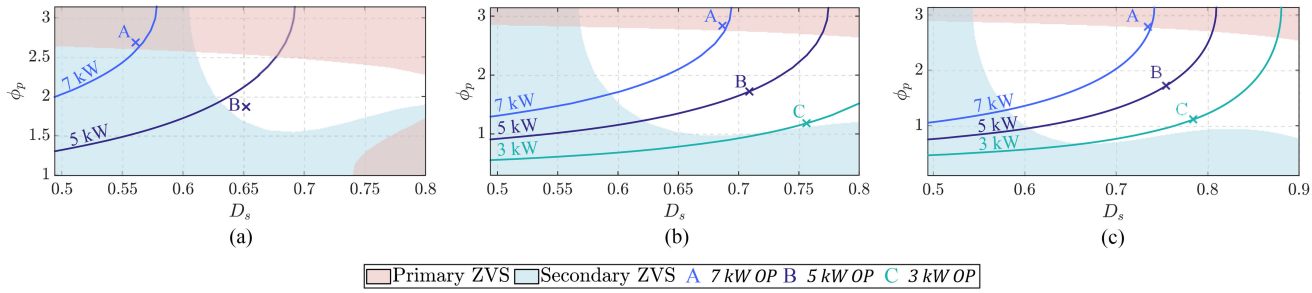

Fig. 12. Selected operating points for various power levels and ZVS turn ON range of the primary full-bridge and secondary IBAB converters as a function of control parameters at locations (a) (75,100,200), (b) (0,0,167), and (c) (0,0,145).

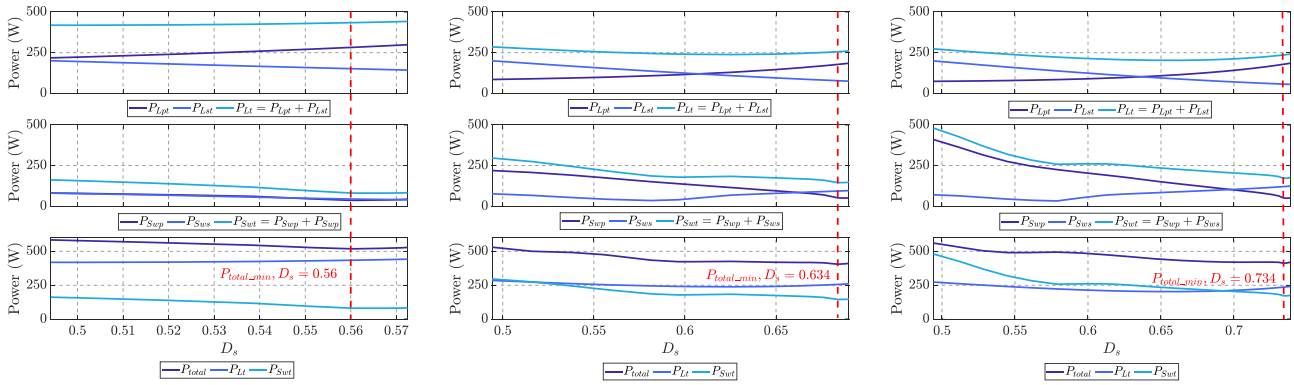

Fig. 13. Primary and secondary magnetic coupler losses (P_{Lpt} and P_{Lst}) and switching device losses (P_{Swp} and P_{Sws}) as a function of D_s for a constant $P_{\mathrm{out}} = 7$ kW at (a) (75,100,200), (b) (0,0,167), and (c) (0,0,145).

TABLE III
CONTROL PARAMETERS @ $P_{\mathrm{out}} = 7$ kW

(X,Y,Z) (mm)	k	V_p	$V_s = 280\ V$		$V_s = 420\ V$	
			ϕ_p	D_s	ϕ_p	D_s
(0,0,125)	0.288	350 V	1.876	61.75%	1.876	73.29%
(0,0,145)	0.237	350 V	1.857	53.11%	2.786	73.45%
(0,0,167)	0.198	350 V	2.836	54.86%	2.836	68.66%
(75,100,167)	0.144	350 V	2.737	34.17%	2.939	57.6%
(75,100,200)	0.110	450 V	3.14	33%	2.683	56.1%

control parameters to be used when regulating the power transfer to 5 and 3 kW, can be determined and are shown in Fig. 12. As evident, the IBAB converter used in the secondary helps to reduce the device stresses typically imposed on the primary full-bridge and as such enhances the power transfer efficiency.

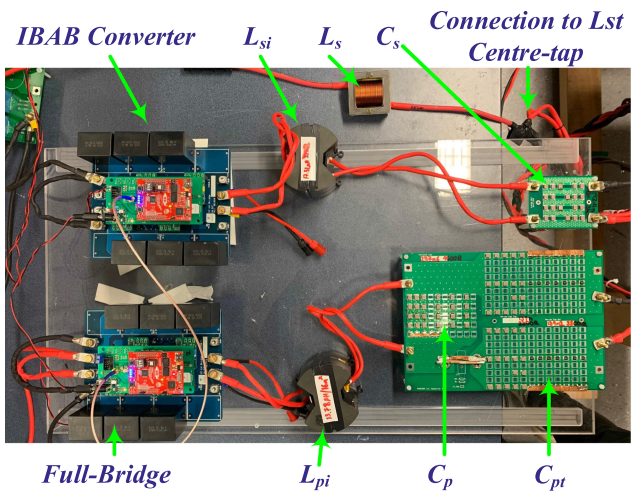

Fig. 14. Photograph of the 7 kW prototype system.

V. EXPERIMENTAL VALIDATION

In order to validate the viability of the proposed IBAB topology and to verify the procedure used to determine the control parameters, experimental voltage and current waveforms of the WPT2/Z2 compliant system were captured at each location specified in Table I.

Fig. 14 shows the constructed prototype system, where L_s is an EK55246-341M-40AH powdered core inductor; L_{pi} and L_{si} are each wound using 4 mm Litz wire ($A_{cu} = 6.4$ mm^2) as two tightly coupled windings (4 turns each) on a TDK N87 PM87/70 core with an air gap of approximately 5.8 and 4 mm, respectively. The tuning capacitor banks used are made up of 100 nF ceramic C5750C0G2J104J280KC capacitors. Note that the design and construction of L_{pi} and L_{si} could have been further optimized to reduce the size and cost. However, since the design presented

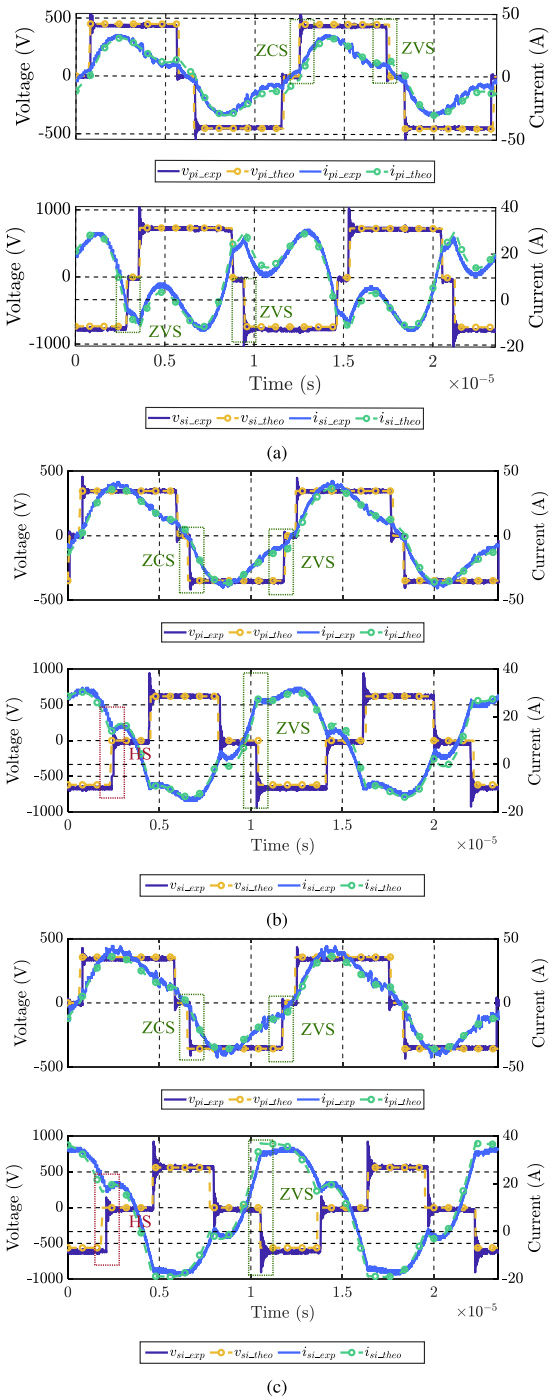

Fig. 15. Experimental and theoretical primary and secondary voltage and current waveforms for the secondary magnetic coupler locations (a) (75, 100, 200), where $k = 0.110$, $P_{\text{out}} = 7$ kW, $V_p = 450$ V, $V_s = 420$ V, $\phi_p = 2.683$, and $D_s = 56.1\%$, (b) (0, 0, 167) where $k = 0.198$, $P_{\text{out}} = 7$ kW, $V_p = 350$ V, $V_s = 420$ V, $\phi_p = 2.836$, and $D_s = 68.66\%$, and (c) (0, 0, 145) where $k = 0.237$, $P_{\text{out}} = 7$ kW, $V_p = 350$ V, $V_s = 420$ V, $\phi_p = 2.786$, and $D_s = 73.45\%$.

is a "proof of concept" system, this was considered to be out of the scope of this article.

As an example, Fig. 15(a)–(c) shows the waveforms captured from the prototype when working under the conditions and

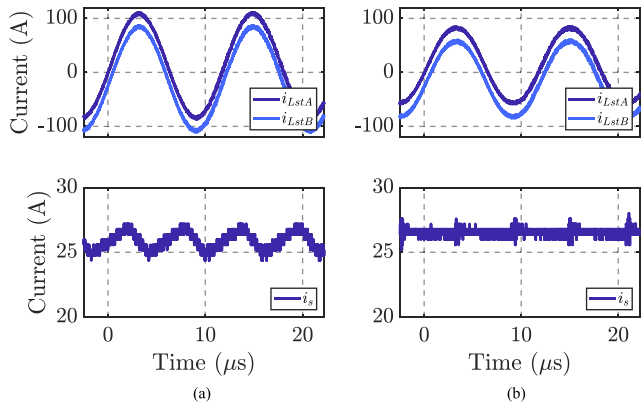

Fig. 16. Experimentally obtained secondary magnetic coupler and dc inductor currents when $P_{\text{out}} = 7$ kW for (a) worst case ripple current and (b) $D_s = 50\%$.

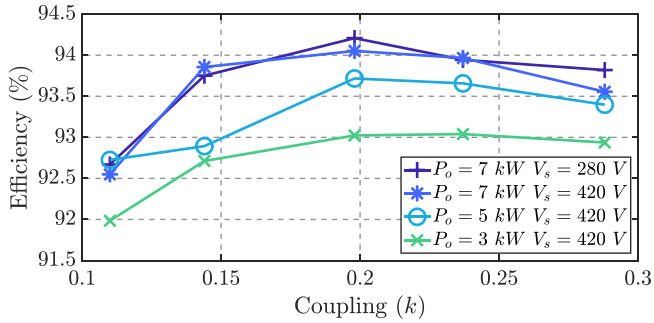

Fig. 17. Experimental dc–dc efficiency of the prototype system for various loading conditions.

control parameters highlighted by the 7-kW operating point shown by Fig. 12(a)–(c), respectively. Experimental waveforms are also overlaid with theoretical waveforms to validate the accuracy of the mathematical models used. Overall, the experimental waveforms present excellent correlation with the switching conditions predicted in Section IV, thus not only verifying the accuracy of the mathematical model used, but also the selection of the various operating points.

In order to verify the reduced dc inductor ripple current and minimum impact to the secondary side magnetic coupler current, I_{Lsta}, I_{Lstb}, and I_s were also captured experimentally and are shown in Fig. 16. The dc inductor, L_s, has a dc-bias of approximately 26 A as the prototype is delivering 7 kW to the output. The inductor ripple current is largest when the coupling and the EV battery voltage are at their lowest. Experimental waveforms when operating under these conditions are shown in Fig. 16(a). Using (14) and approximating L_{cm} as L_s, the peak ripple current can be calculated as 1.12 A, which correlates well with the experimental results. When the secondary coupler is at (0,0,167) and $V_s = 280$ V, D_s is approximately 50%. As predicted by (14) and depicted in Fig. 16(b), under these conditions, ΔI_{sicm_pk} is nearly 0. It is also apparent that the dc current splits equally between the two windings of the secondary magnetic coupler, which presents very low distortion.

As presented by Fig. 17, the proposed system achieves very good dc–dc efficiency over the full coupling range and EV

battery voltage range. The prototype maintains efficiency over 92% even when regulating the output power down to 3 kW as required by the EV battery management system. The overall variation in efficiency is minimal, ranging from 92% to 94.2%. The best efficiency is achieved when the coupling is approximately 0.2 since this position achieves a good balance between the magnetic coupler losses and the converter losses. The efficiency is lower when the coupling is low due to the magnetic coupler losses that dominate the overall losses. On the other hand, when the coupling is high, both ϕ_p and D_s need to be modulated; thus converter losses tend to dominate, leading to a reduction in efficiency.

VI. Conclusion

This article presented a novel BAB converter, which integrated the current splitting functionality previously achieved using two dc inductors into a DD magnetic coupler. The advantages of this converter, such as reduced conduction losses, a large ZVS turn-ON range and a reduction in magnetic components were discussed in detail. The proposed IBAB converter was utilized as the secondary side converter for an SAE J2954 WPT2/Z2 compliant EV charging system to highlight its advantages. This article also detailed the methodology used to select control parameters for various positions of the secondary coupler within the operating region specified by the standard. In order to validate the presented models and verify the improved performance of the proposed system, a 7-kW "proof of concept" prototype was designed and built. The experimental results highlighted how the IBAB converter relieved regulation stress from the primary full-bridge converter and benefited the overall system efficiency. The experimental system efficiency was between 94.2% and 92%, varying by just 1.7% when subjected to a coupling change of +/− 43.5% (0.11 to 0.28) and the full battery voltage variation specified by the SAE J2954 WPT2/Z2 standard.

References

[1] G. A. Covic and J. T. Boys, "Modern trends in inductive power transfer for transportation applications," *IEEE J. Emerging Sel. Topics Power Electron.*, vol. 1, no. 1, pp. 28–41, Mar. 2013.

[2] R. Bosshard and J. W. Kolar, "Inductive power transfer for electric vehicle charging: Technical challenges and tradeoffs," *IEEE Power Electron. Mag.*, vol. 3, no. 3, pp. 22–30, Sep. 2016.

[3] C. C. Mi, G. Buja, S. Y. Choi, and C. T. Rim, "Modern advances in wireless power transfer systems for roadway powered electric vehicles," *IEEE Trans. Ind. Electron.*, vol. 63, no. 10, pp. 6533–6545, Oct. 2016.

[4] A. Zaheer, G. A. Covic, and D. Kacprzak, "A bipolar pad in a 10-kHz 300-W distributed IPT system for AGV applications," *IEEE Trans. Ind. Electron.*, vol. 61, no. 7, pp. 3288–3301, Jul. 2014.

[5] M. J. Chabalko and A. P. Sample, "Three-dimensional charging via multimode resonant cavity enabled wireless power transfer," *IEEE Trans. Power Electron.*, vol. 30, no. 11, pp. 6163–6173, Nov. 2015.

[6] P. Si, A. P. Hu, S. Malpas, and D. Budgett, "A frequency control method for regulating wireless power to implantable devices," *IEEE Trans. Biomed. Circuits Syst.*, vol. 2, no. 1, pp. 22–29, Mar. 2008.

[7] R. Bosshard and J. W. Kolar, "Multi-objective optimization of 50 kw/85 kHz IPT system for public transport," *IEEE J. Emerging Sel. Topics Power Electron.*, vol. 4, no. 4, pp. 1370–1382, Dec. 2016.

[8] Z. Huang, S. Wong, and C. K. Tse, "Design of a single-stage inductive-power-transfer converter for efficient EV battery charging," *IEEE Trans. Veh. Technol.*, vol. 66, no. 7, pp. 5808–5821, Jul. 2017.

[9] F. Lu, H. Zhang, T. Kan, H. Hofmann, Y. Mei, L. Cai, and C. Mi, "A high efficiency and compact inductive power transfer system compatible with both 3.3 kW and 7.7 kW receivers," in *Proc. IEEE Appl. Power Electron. Conf. Expo.*, Mar. 2017, pp. 3669–3673.

[10] J. Deng, F. Lu, S. Li, T. Nguyen, and C. Mi, "Development of a high efficiency primary side controlled 7 kW wireless power charger," in *Proc. IEEE Int. Electric Vehicle Conf.*, Dec. 2014, pp. 1–6.

[11] D. J. Thrimawithana and U. K. Madawala, "A generalized steady-state model for bidirectional IPT systems," *IEEE Trans. Power Electron.*, vol. 28, no. 10, pp. 4681–4689, Oct. 2013.

[12] A. Zaheer, M. Neath, H. Z. Z. Beh, and G. A. Covic, "A dynamic EV charging system for slow moving traffic applications," *IEEE Trans. Transp. Electrification*, vol. 3, no. 2, pp. 354–369, Jun. 2017.

[13] W. Kempton and J. Tomi," Vehicle-to-grid power fundamentals: Calculating capacity and net revenue," *J. Power Sources*, vol. 144, no. 1, pp. 268–279, 2005.

[14] G. R. Kalra, C. Y. Huang, D. J. Thirmawithana, U. K. Madawala, and M. Neuburger, "A comparative study on grid-integration techniques used in bi-directional IPT based v2g applications," in *Proc. IEEE 2nd Annu. Southern Power Electron. Conf.*, 2016, pp. 1–6.

[15] "Wireless power transfer for light-duty plug-in/electric vehicles and alignment methodology," SAE International, Tech. Rep. J2954_201904, 2016.

[16] "Electric vehicle wireless power transfer (WPT) systems - Part 1: General requirements," International Electrotechnical Commission, Geneva, CH, Standard, Jul. 2015.

[17] M. Budhia, J. T. Boys, G. A. Covic, and C. Huang, "Development of a single-sided flux magnetic coupler for electric vehicle IPT charging systems," *IEEE Trans. Ind. Electron.*, vol. 60, no. 1, pp. 318–328, Jan. 2013.

[18] H. L. Li, A. P. Hu, G. A. Covic, and C. Tang, "A new primary power regulation method for contactless power transfer," in *Proc. IEEE Int. Conf. Ind. Technol.*, Feb. 2009, pp. 1–5.

[19] H. H. Wu, A. Gilchrist, K. Sealy, P. Israelsen, and J. Muhs, "Design of symmetric voltage cancellation control for LCL converters in inductive power transfer systems," in *Proc. IEEE Int. Electric Mach. Drives Conf.*, May 2011, pp. 866–871.

[20] D. Perreault and A. S. Jurkov, "Tunable matching network with phase-switched elements," U.S. Patent 9 755 576B2, Jun. 23, 2016.

[21] J. T. Boys, G. A. Covic, and A. W. Green, "Stability and control of inductively coupled power transfer systems," *IEE Proc. Electric Power Appl.*, vol. 147, no. 1, pp. 37–43, 2000.

[22] H. H. Wu, A. Gilchrist, K. D. Sealy, and D. Bronson, "A high efficiency 5 kw inductive charger for EVS using dual side control," *IEEE Trans. Ind. Informat.*, vol. 8, no. 3, pp. 585–595, Aug. 2012.

[23] C. Huang, J. T. Boys, and G. A. Covic, "LCL pickup circulating current controller for inductive power transfer systems," *IEEE Trans. Power Electron.*, vol. 28, no. 4, pp. 2081–2093, Apr. 2013.

[24] K. Colak, M. Bojarski, E. Asa, and D. Czarkowski, "A constant resistance analysis and control of cascaded buck and boost converter for wireless EV chargers," in *Proc. IEEE Appl. Power Electron. Conf. Expo.*, Mar. 2015, pp. 3157–3161.

[25] H. Z. Z. Beh, M. Neath, G. A. Covic, and J. T. Boys, "Evaluation of a current doubler IPT pickup controller for materials handling applications," in *Proc. IEEE 2nd Annu. Southern Power Electron. Conf.*, Dec. 2016, pp. 1–6.

[26] T. Diekhans and R. W. De Doncker, "A dual-side controlled inductive power transfer system optimized for large coupling factor variations and partial load," *IEEE Trans. Power Electron.*, vol. 30, no. 11, pp. 6320–6328, Nov. 2015.

[27] G. Kalra, D. J. Thrimawithana, B. S. Riar, C. Huang, and M. Neuburger, "A novel boost active bridge based inductive power transfer system," *IEEE Trans. Ind. Electron.*, vol. 67, no. 2, pp. 1103–1112, Feb. 2020.

[28] S. Li, W. Li, J. Deng, T. D. Nguyen, and C. C. Mi, "A double-sided LCC compensation network and its tuning method for wireless power transfer," *IEEE Trans. Veh. Technol.*, vol. 64, no. 6, pp. 2261–2273, Jun. 2015.

[29] X. Zhang *et al.*, "A control strategy for efficiency optimization and wide ZVS operation range in bidirectional inductive power transfer system," *IEEE Trans. Ind. Electron.*, vol. 66, no. 8, pp. 5958–5969, Aug. 2019.

[30] A. Reatti and M. K. Kazimierczuk, "Comparison of various methods for calculating the AC resistance of inductors," *IEEE Trans. Magn.*, vol. 38, no. 3, pp. 1512–1518, May 2002.

[31] D. Costinett, D. Maksimovic, and R. Zane, "Circuit-oriented treatment of nonlinear capacitances in switched-mode power supplies," *IEEE Trans. Power Electron.*, vol. 30, no. 2, pp. 985–995, Feb. 2015.

Gaurav R. Kalra (Student Member, IEEE) received the B.E. (hons.) degree in electrical and electronic engineering in 2016 from The University of Auckland, Auckland, New Zealand, where he is currently working toward the Ph.D. degree.

His research interests include power electronics, inductive power transfer, and renewable energy technology.

Baljit S. Riar received the B.E. (hons.) and Ph.D. degrees in electrical and electronic engineering from The University of Auckland, Auckland, New Zealand, in 2010 and 2015, respectively.

He is currently working with United Technologies Research Center (UTRC), as a Senior Research Engineer. Prior to joining UTRC, he worked as a Postdoctoral Fellow with Utah State University, and as a Postdoctoral Researcher with the University of Oxford, Oxford, U.K. His main areas of research include design and control of power converters, battery management systems, wireless power transfer systems, microgrid systems, and model predictive control.

Duleepa J. Thrimawithana (Senior Member, IEEE) received the B.E. (with first class hons.) degree in electrical engineering and the Ph.D. degree in power electronics from The University of Auckland, Auckland, New Zealand, in 2005 and 2019, respectively.

In 2009, he joined the Department of Electrical and Computer Engineering, The University of Auckland, in 2009 where he currently works as a Senior Lecturer. He has coauthored more than 100 international journal and conference publications, and has filled 14 patents on wireless power transfer technologies. His main research areas include wireless power transfer, power electronics, and renewable energy.

Dr. Thrimawithana serves as the Chairman of the Joint Chapter of IEEE Industrial Electronics and Industrial Applications Society, New Zealand (North). He was the recipient of the Jim and Hazel D. Lord Fellowship in 2014.